


Article

Structural, Electronic, and Optical Properties of Group 6 Doped Anatase TiO₂: A Theoretical Approach

Petros-Panagis Filippatos ^{1,2,*}, Nikolaos Kelaidis ^{2,3}, Maria Vasilopoulou ^{1,*}, Dimitris Davazoglou ¹ and Alexander Chroneos ^{2,4,*} 

- ¹ National Center for Scientific Research Demokritos, Institute of Nanoscience and Nanotechnology (INN), Agia Paraskevi, 15310 Athens, Greece; d.davazoglou@inn.demokritos.gr
- ² Faculty of Engineering, Environment and Computing, Coventry University, Priory Street, Coventry CV1 5FB, UK; ad1978@coventry.ac.uk
- ³ Theoretical and Physical Chemistry Institute, National Hellenic Research Foundation, Vass. Constantinou 48, 11635 Athens, Greece
- ⁴ Department of Materials, Imperial College, London SW7 2AZ, UK
- * Correspondence: petpanfilippatos@gmail.com (P.-P.F.); m.vasilopoulou@inn.demokritos.gr (M.V.); alexander.chroneos@imperial.ac.uk (A.C.)

Abstract: Titania (TiO₂) is a key material used as an electron transport in dye-sensitized and halide perovskite solar cells due to its intrinsic n-type conductivity, visible transparency, low-toxicity, and abundance. Moreover, it exhibits pronounced photocatalytic properties in the ultra-violet part of the solar spectrum. However, its wide bandgap (around 3.2 eV) reduces its photocatalytic activity in the visible wavelengths' region and electron transport ability. One of the most efficient strategies to simultaneously decrease its bandgap value and increase its n-type conductivity is doping with appropriate elements. Here, we have investigated using the density functional theory (DFT), as well as the influence of chromium (Cr), molybdenum (Mo), and tungsten (W) doping on the structural, electronic, and optical properties of TiO₂. We find that doping with group 6 elements positively impacts the above-mentioned properties and should be considered an appropriate method for photocatalytic applications. In addition to the pronounced reduction in the bandgap values, we also predict the formation of energy states inside the forbidden gap, in all the cases. These states are highly desirable for photocatalytic applications as they induce low energy transitions, thus increasing the oxide's absorption within the visible. Still, they can be detrimental to solar cells' performance, as they constitute trap sites for photogenerated charge carriers.



Citation: Filippatos, P.-P.; Kelaidis, N.; Vasilopoulou, M.; Davazoglou, D.; Chroneos, A. Structural, Electronic, and Optical Properties of Group 6 Doped Anatase TiO₂: A Theoretical Approach. *Appl. Sci.* **2021**, *11*, 1657. <https://doi.org/10.3390/app11041657>

Academic Editor: Marco Anni

Received: 18 January 2021

Accepted: 8 February 2021

Published: 12 February 2021

Publisher's Note: MDPI stays neutral with regard to jurisdictional claims in published maps and institutional affiliations.



Copyright: © 2021 by the authors. Licensee MDPI, Basel, Switzerland. This article is an open access article distributed under the terms and conditions of the Creative Commons Attribution (CC BY) license (<https://creativecommons.org/licenses/by/4.0/>).

Keywords: anatase TiO₂; Cr; Mo; W doping; semiconductor; photocatalytic materials

1. Introduction

Transition metal oxides such as TiO₂, tin oxide (SnO₂), and zinc oxide (ZnO) represent an important class of materials due to their chemical stability, photocatalytic properties, and high electrical conductivity [1–10]. Anatase TiO₂ has been widely investigated as a photocatalyst and as a solar cell material due to its intense absorption in the ultra-violet wavelength region [1–7]. Furthermore, it has been long established as an effective electron transport layer (ETL) in dye-sensitized solar cells (DSSCs) and recently in organic (OSCs) and perovskite solar cells (PSCs) [8–25]. The bandgap of anatase TiO₂, which is around 3.2 eV [26,27], reduces its absorption in the near-infrared and visible region [7]. To decrease its bandgap and tune the electronic and optical properties, doping with appropriate elements is beneficial. A considerable variety of literature reports demonstrate that doping of anatase TiO₂ with halogens, nitrogen, or transition metal ions such as zinc (Zn) significantly changes the electronic and optical properties [28–34]. For instance, when we dope TiO₂ with chlorine (Cl) or nickel (Ni), the bandgap is reduced to 3 and 2.6 eV, respectively [33,34].

Although TiO₂ has been investigated for many years as a photocatalyst, in the anatase form it undergoes fast electron-hole recombination, leading to unsatisfactory photocatalytic

properties [26,27]. Many doping strategies have been adopted, such as nitrogen (N) and niobium (Nb) doping, which resulted in the enhanced photocatalytic activity of TiO₂ [35,36]. Herein, we investigate the chromium (Cr), molybdenum (Mo), and tungsten (W) (group 6 of the periodic table) doping of anatase TiO₂ using the density functional theory (DFT). We focus on the structural, electronic, and optical properties of anatase TiO₂ before and after doping with the group 6 elements and we provide evidence that these structures can be applicable to photocatalytic applications and devices. Furthermore, we compare our results with already published experimental data and theoretical results referring to other dopants. To fully understand the structural and electronic properties changes, we considered the density of states (DOS) of the energetically favorable sites and the partial DOS (PDOS) for the orbital contribution. To our knowledge, the orbitals hybridization of the interstitial and substitutional doping cases, has not been systematically discussed before. Finally, we calculated the absorption, refractive index, and dielectric constants for these dopants. In this work, we made a complete investigation both for the substitutional and the interstitial doping cases, to serve as a roadmap to the applications of TiO₂ to photocatalysis and photoelectrical devices.

2. Materials and Methods

For all the DFT calculations presented here, we use the plane wave code CASTEP [37,38], with the PBE [39] exchange-correlation functional. Furthermore, the ultrasoft pseudopotentials [40] were used for all of our calculations. The wave basis's cut-off energy was converged at 480 eV, in conjunction with a $2 \times 2 \times 3$ k-point Monkhost-Pack [41] grid. For our calculations, we used a supercell of 108 atoms. To encounter the effect of localized electrons, onsite Coulomb repulsions [42] of 8.2 eV were set for the 3d orbitals of Ti [15], 2.8 eV for the 3d of Cr [43], 2.3 eV for Mo 4d, and 2.1 eV for W 5d [44]. We have also examined other values for the +U parameter, but the band gap was significantly underestimated. For the DOS calculations, a denser mesh of $5 \times 5 \times 5$ k-points was applied. The convergence criteria for the undoped TiO₂ and doped structures were chosen as (a) the SCF tolerance of 2.0×10^{-5} eV/atom, (b) max force tolerance of 0.05 eV/Å, (c) max stress tolerance of 0.1 GPa, and d) max displacement tolerance of 0.001 Å. For the optical calculations, a denser mesh of $3 \times 3 \times 3$ k-points was applied.

3. Results

3.1. Structural and Electronic Properties

Among the three different crystal structures of TiO₂ (brookite, rutile, and anatase), anatase is considered the most suitable for photocatalytic devices [45]. It belongs to the tetragonal I4/amd space group and its lattice parameters are measured to be $a = 3.782$ Å, $b = 3.782$ Å, and $c = 9.502$ Å [46]. Herein, the DFT calculated lattice parameters are $a = 3.804$ Å, $b = 3.804$ Å, and $c = 9.729$ Å, which agree with previous theoretical studies [8,34,47]. The dopants' percentage was 1 X (=Cr, Mo, W) atom per 108 TiO₂ atoms, which results in a 0.92% doping percentage. In our work, all the dopants were examined in interstitial and substitutional positions. We discuss the effect of the above dopants for interstitial and Ti-substitutional doping. Each case produces a small distortion in the lattice, which changes the crystal parameters and the supercell volume (Table 1). The increase of the unit cell volume is due to the electronegativity differences between Mo, W, and Ti. This is in turn reflected on the larger Ti-X(=Mo, W) distance as compared to the Ti-Ti distance of the undoped TiO₂.

3.1.1. Cr Doping

In the case of Cr_i, the chromium atom resides at 2.25 Å from the nearest titanium atom and 2.25 Å from the nearest oxygen atom (Figure 1a). Furthermore, we have also examined the Ti simple substitution with Cr and present the relaxed structure in Figure 1b. In this case, the Cr atom resides 1.91 Å from the nearest oxygen atom. For the substitutional case, the lattice parameters are reduced. Our results agree with other available theoretical

and experimental data [48,49], which predict a decrease in the cell volume due to the Cr incorporation in a substitutional position.

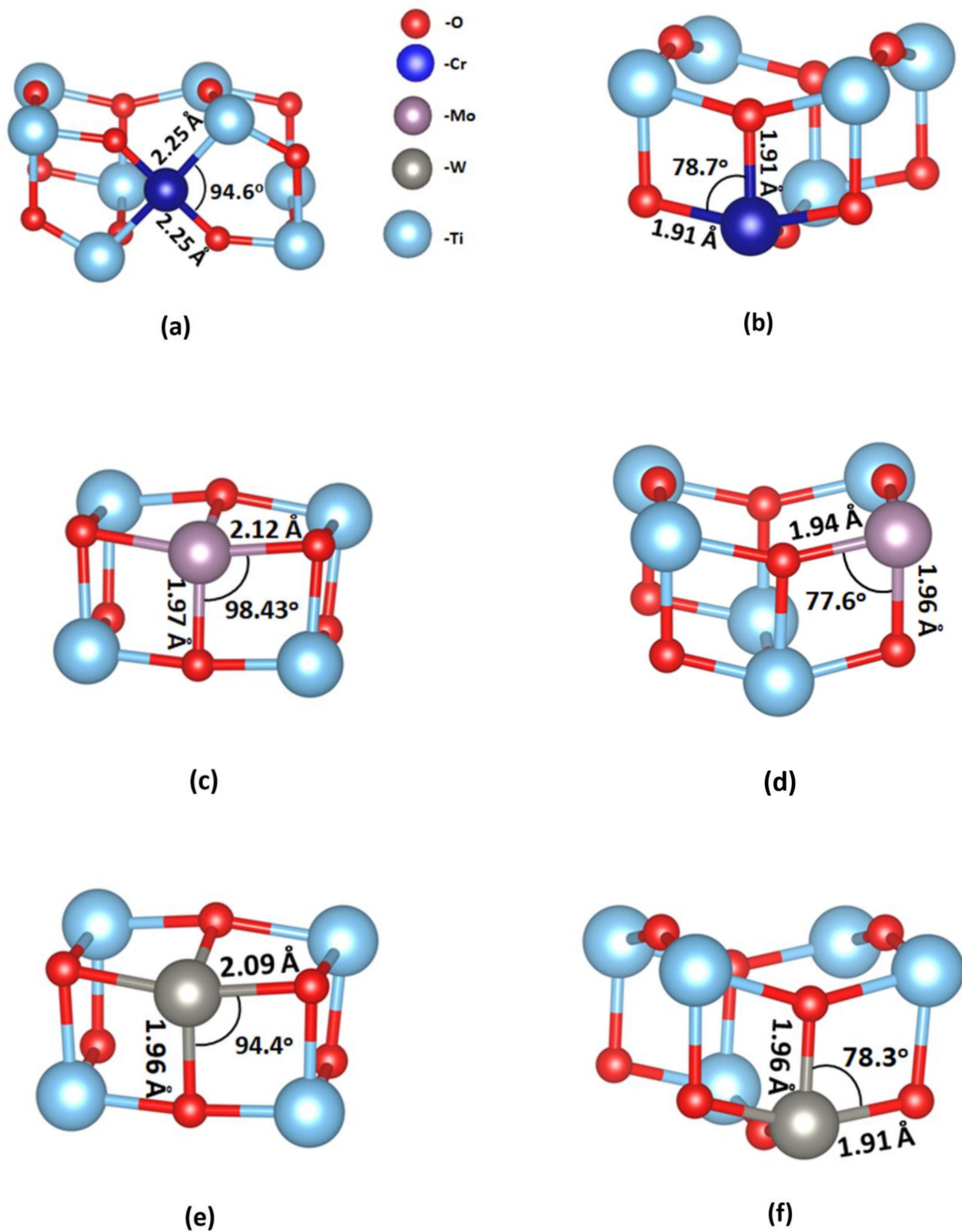


Figure 1. (a) Chromium (Cr) as an interstitial dopant, (b) Cr as a substitutional dopant, (c) molybdenum (Mo) as an interstitial dopant, (d) Mo as a substitutional dopant, (e) tungsten (W) as an interstitial dopant, (f) W as a substitutional dopant.

Table 1. Lattice parameters and cell volume for every doping case.

	a (Å)	c (Å)	Volume (Å ³)
TiO ₂	3.80	9.73	140.80
Cr _i :TiO ₂	3.80	9.80	143.75
Cr _{Ti} :TiO ₂	3.81	9.69	140.29
Mo _i :TiO ₂	3.83	9.70	142.29
Mo _{Ti} :TiO ₂	3.81	9.72	141.10
W _i :TiO ₂	3.83	9.70	142.30
W _{Ti} :TiO ₂	3.82	9.69	141.40

Focusing on the DOS graph, the bandgap is estimated at 3.04 eV for the Cr_i and 3.09 eV for the Cr_{Ti} cases (Figure 2a,b). The bandgap of perfect anatase is calculated at 3.12 eV (shown in Figure 2g as a reference), which agrees with other theoretical studies and already published reports that show experimental values for the bandgap at 3.2 eV [27,33,34,50].

As shown in Figure 2a, the Cr interstitial gives rise to three available energy states inside the bandgap, near the valence band edge, in the middle of the bandgap, and near 2.5 eV. However, when a Ti atom is replaced with Cr, it is observed that the gap states are shifted towards the conduction band (Figure 2b). To fully explain the hybridizations that create these gap states, we used the PDOS for the Cr_i:TiO₂ and Cr_{Ti}:TiO₂. Figure 3a shows that O-2p and Ti-3d contribute mainly to the valence and the conduction band, respectively. Furthermore, the interstitial Cr doping mainly contributes to gap states with a minor contribution also as the conduction band.

In Figure 3a, the gap states are shown in more detail. The bandgap states are formed at 0.32 eV, which is attributed to the hybridization of O-2p, Ti-3d, and Cr-3d orbitals, with O-2p contributing more to this state. The gap state at 1.25 eV has a contribution of Ti-3d, O-2p, and Cr-4s orbitals. The energy states at 2.4 eV are created from the hybridization of Cr-3d with Ti-3d orbitals. The results are in good agreement with other theoretical works [51]. In Figure 3b, the Cr_{Ti}:TiO₂ case is examined. The substitutional doping of Cr creates three gap states inside the bandgap and one state at the conduction band edge and also reduces the bandgap to 3.08 eV.

Regarding the origin of gap states (Figure 3b), our calculations predict that they are mainly created due to the hybridization of Cr-3d with Ti-3d and O-2p orbitals. Similar theoretical and experimental works predict a bandgap close to the present value for the same doping percentage [48,52].

3.1.2. Mo Doping

Concerning the doping of TiO₂ with Mo atoms, we show that Mo can be either an interstitial at 1.97 Å from the nearest oxygen or a Ti substitutional at a 1.94 Å distance from the nearest oxygen (Figure 1c,d, respectively).

For the interstitial doping, the DOS in Figure 2c shows peaks in the bandgap at 0.4, 1.2, 1.4, and 1.75 eV. Moreover, the bandgap is decreased to 2.87 eV. Focusing on the PDOS (Figures 2c and 3c), we see that the bandgap available states are mainly created from the Ti-3d and O-2p orbitals. For the gap states at 0.4 eV, we observe a small contribution from the Mo-4d orbitals. We have also predicted that the Mo-4d orbitals create energy states near the conduction band edge. For the substitutional case, mid-gap states are formed at 1.6 eV (Figure 2d). Figure 3d shows that these gap states are created from the hybridization of Ti-3d with O-2p with a small contribution of Mo-4d. However, similarly to the interstitial doping, available states are formed near the conduction band mainly from Mo-4d and Ti-3d orbitals. For the substitutional case, however, our bandgap is reduced to 2.77 eV. The present results for the substitutional doping are consistent with previous theoretical studies [53], however, we could not find any relevant work for the interstitial

case. Sreedhar et al. [54] and Kubaska et al. [55] performed experiments regarding the Mo doped TiO₂ and estimated a bandgap ranging from 2.65 to 3.0 eV.

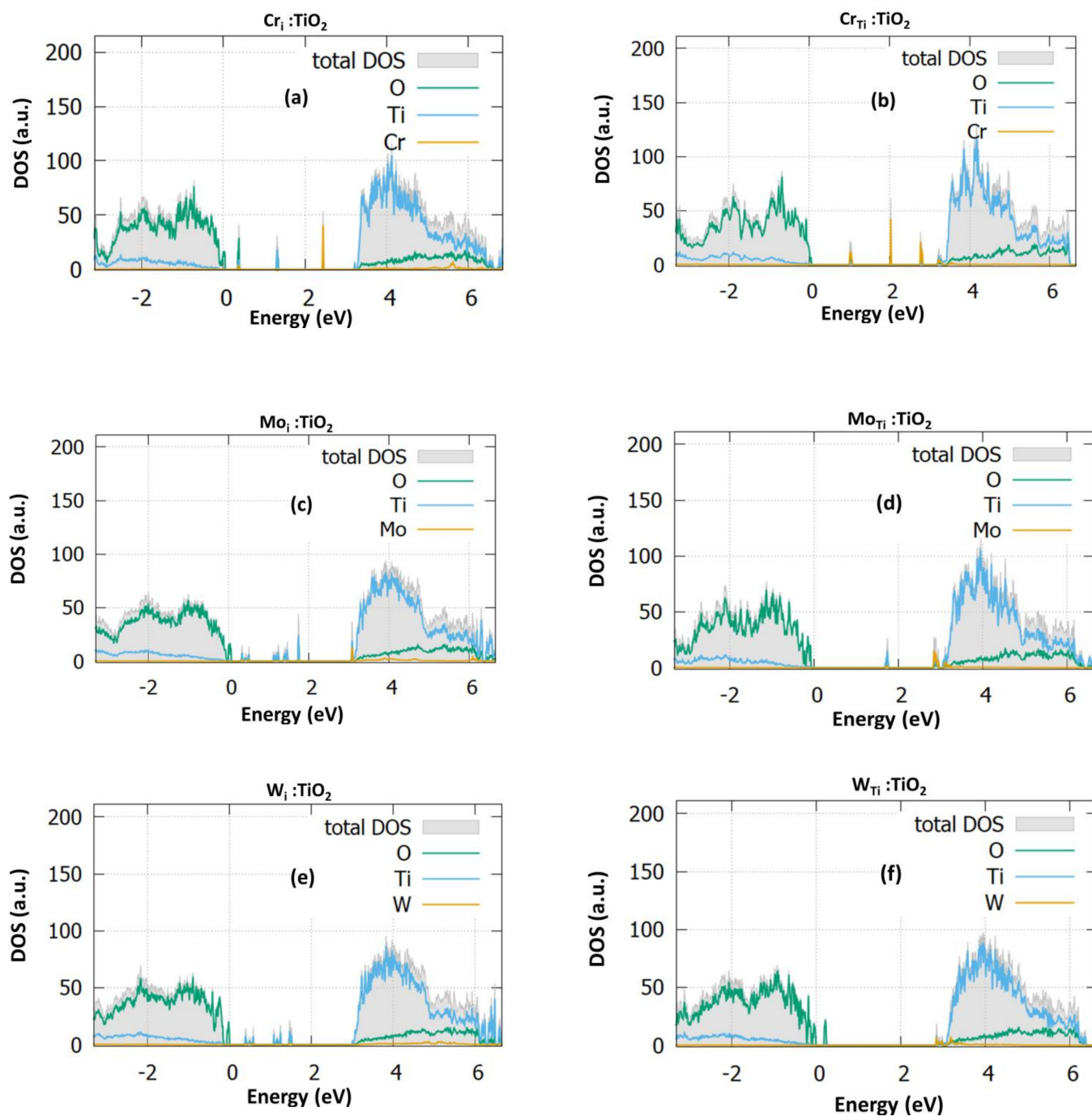


Figure 2. Cont.

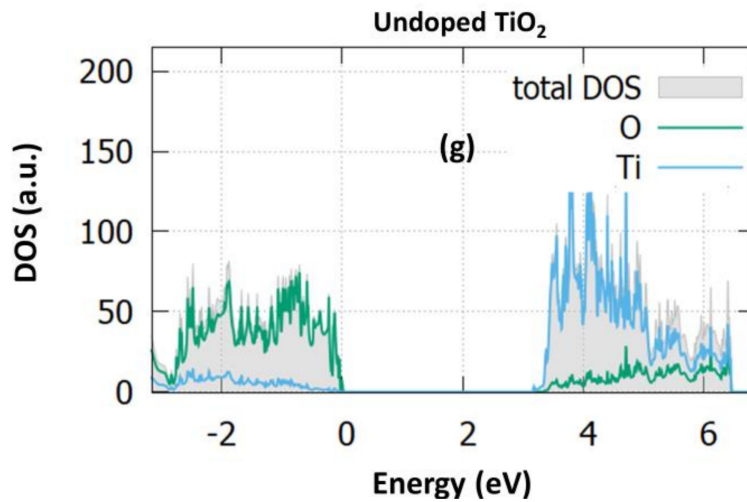


Figure 2. The partial density of states for (a) Cr as an interstitial dopant, (b) Cr as a substitutional dopant, (c) Mo as an interstitial dopant, (d) Mo as a substitutional dopant, (e) W as an interstitial dopant, (f) W as a substitutional dopant, (g) undoped TiO₂.

3.1.3. W Doping

In Figure 1e,f we present the W:TiO₂. In this case, the interstitial sits at 1.96 Å near the oxygen atom, while the substitutional is located at 1.91 Å near the O-atom.

We have also examined the electrical properties of W:TiO₂ both as interstitial and substitutional defects. Specifically, with regards to W_i:TiO₂, in Figure 2e we predict that some mid-gap states are formed and the bandgap is significantly reduced, reaching a value of 2.8 eV. To analyze these states, in Figures 2e and 3e, we observe that three gap states are formed at 0.4–0.6 eV, 1.1–1.3 eV, and 1.5 eV and are mainly created from the Ti-3d and O-2p orbitals. In this case, we compute that the W-4d orbitals contribute significantly neither to the gap states, nor to the conduction band.

Conversely, examining the DOS and PDOS (Figures 2f and 3f) of the substitutional doping case, we observe that the W-5d orbitals create some available states near the conduction band, which reduce the bandgap to the value of 2.87 eV. In addition, some states are formed at 0.1 eV, which result from the O-2p and Ti-3d orbitals. Our band gap calculations are in good agreement with the experiments, which predict a value of 2.9 eV [56].

In Table 2, we have summarized our results. Our calculations indicate that the gap is reduced more in Mo_{Ti} doped TiO₂ and reaches a value of 2.77 eV (448 nm). Therefore, it is suggested that this type of bandgap engineering of titania can be applied to develop photocatalysts with an absorption within the visible. Generally, in all the above cases, we calculate a significant bandgap reduction. Additionally, we have extensively discussed the creation of gap states in the middle of the bandgap for all the doping cases. These formed states improve the n-type conductivity of titania and serve as donors. As a result, we suggest that their photocatalytic performance through water splitting experiments should be examined, especially for the Mo doping. Although these states can be advantageous for photocatalytic applications, they could be a disadvantage for solar cell devices, as they might constitute trap sites for the photogenerated charge carriers. As a result, we propose only the W doped TiO₂ for application in photovoltaics.

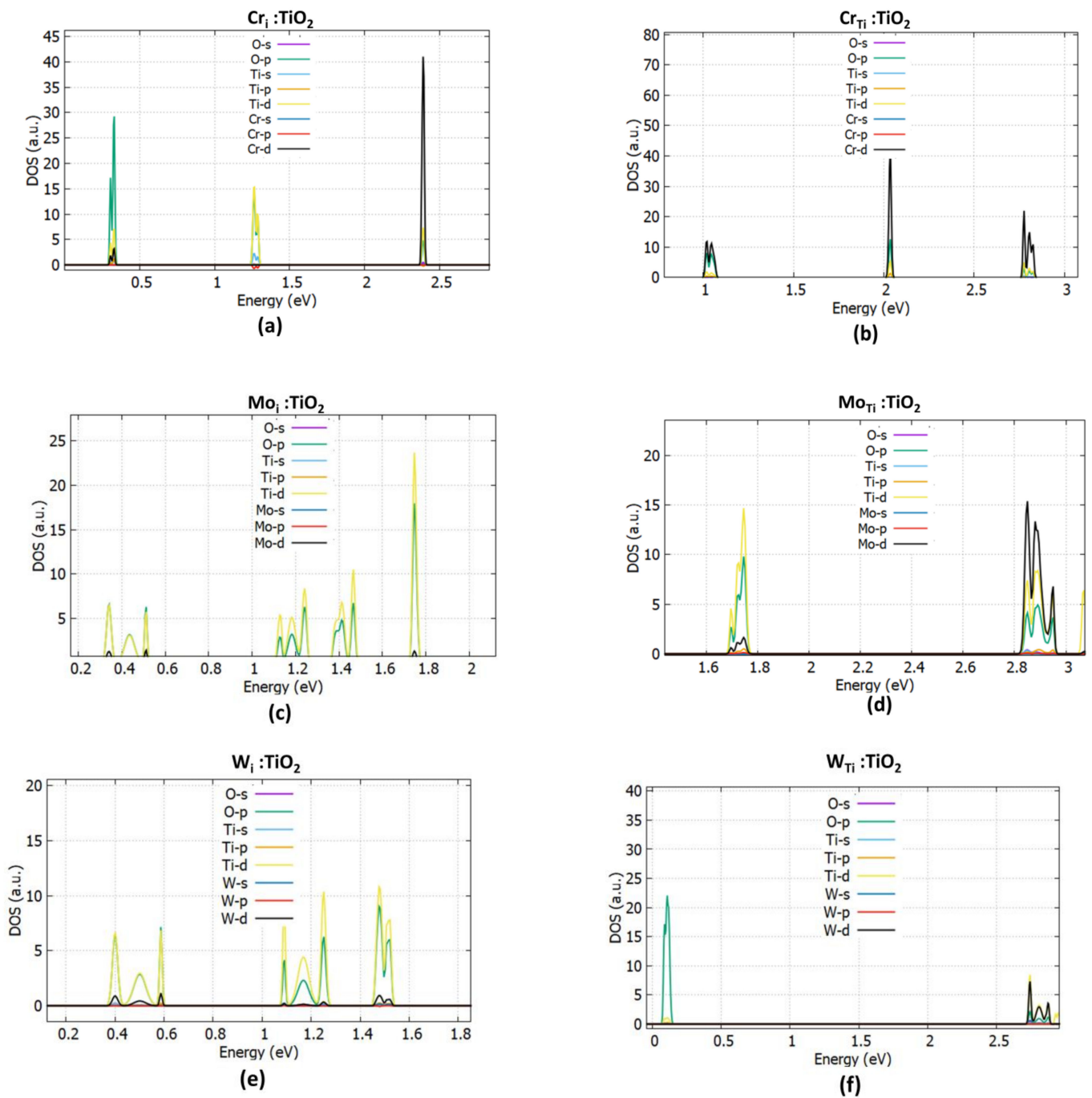


Figure 3. The mid gap states for (a) Cr as an interstitial dopant, (b) Cr as a substitutional dopant, (c) Mo as an interstitial dopant, (d) Mo as a substitutional dopant, (e) W as an interstitial dopant, (f) W as a substitutional dopant.

Table 2. The calculated band gap values for every interstitial and substitutional doping case.

	Band Gap (eV)
TiO ₂	3.12
Cr _i :TiO ₂	3.04
Cr _{Ti} :TiO ₂	3.09
Mo _i :TiO ₂	2.87
Mo _{Ti} :TiO ₂	2.77
W _i :TiO ₂	2.89
W _{Ti} :TiO ₂	2.88

3.2. Optical Properties

The optical properties for the absorption coefficient, refractive index, and dielectric function were analyzed for the undoped and the X(=Cr, Mo, W):TiO₂ substitutional cases. In the optical calculations, we used the Hubbard + U parameter and concluded that the present results are in good agreement with the experiment, although they are highly dependent on this parameter. In Figure 4a–f, the complex dielectric function is presented for photon energies up to 15 eV. In Figure 4g, the dielectric function of the undoped case is shown. The dielectric constant ϵ_{00} is predicted in the limit of zero photon energy of the real part of the dielectric function, at 5. This agrees well with other computational works, which predict a value of 5.10 [57] and slightly higher than the experimental value of 4.5 [58]. The imaginary part of the dielectric function for the undoped case shows a peak at about 5 eV. This peak is in good agreement with the literature [57] and was attributed to the electronic transition from Ti-3d to O-2p states at the conduction and the valence band. For the Cr doping case, the dielectric function is presented in Figure 4a. The dielectric constant is calculated at the value of 6 from the real part of the dielectric function. From the imaginary part of the dielectric function, we show that it has a similar form to the pure TiO₂. In Figure 4b, the dielectric function for the Mo:TiO₂ is presented. Focusing on the real part, the dielectric constant is estimated at the value of 9. From the imaginary part, a peak in the low region is created (0.31 eV), which comes from the electronic intra-band transition of Mo 4d and Ti-3d orbitals inside the conduction band. The present results are similar with other theoretical works [59,60]. For the W-case, we predict the dielectric constant at 6. As for the imaginary part, it is seen that 0.23 eV is created from the W-4d transition with the Ti-3d in the conduction band.

The computed refractive index value for the undoped TiO₂ is 2.35. The present results agree with other theoretical studies that calculate a value of 2.21 [57]. Mergel [61], performed experiments and estimated that the refractive index of undoped TiO₂ is computed at the value of 2.62 at 550 nm. Here, we calculate a value of 2.62 at 550 nm (which is equal to an energy of 2.25 eV), identical to the experimental value. The imaginary part of the refractive index corresponds to the extinction coefficient. The significant peaks from the extinction coefficient are located at 5.30, which is close to other provided values [57]. It is seen that the real part of the refractive index gives a value of 2.44 for zero photon energy. The available experimental data predict a value of 2.40, which is similar with our data [62]. From the real part of the refractive index of the Mo:TiO₂, we observe that at the zero photon energy, the index is calculated near 4. This is a significant increase compared to the undoped case. Similar to the present study, Khan et al. [60] also showed an increase of 1.5 units to the refractive index, after the 0.92% doping of Mo to the pure TiO₂. An increase in the refractive index of TiO₂ upon Mo doping boosts its anti-reflective (AR) ability and might be beneficial for application in solar harvesting devices. For the extinction coefficient, $k(\omega)$, in this case, it is seen that a strong peak is created at 5.2 eV. Finally, with regards to the W doped TiO₂, from the real part of the refractive index, it is seen that at zero photon energy, the index is calculated at 2.40, almost equal to the experimental value of 2.3 provided by Lin [63].

We present the absorption coefficient $a(\omega)$ in Figure 5. The major peak ranges from 2.5 to 12.3 eV for the undoped TiO_2 , which is in good agreement with other works [57]. Pure TiO_2 only shows absorption in the UV region, created from the excitations from the O-2p states of the valence band to the Ti-3d states to the conduction band. It is seen that after doping, Mo gives the most substantial peak at 0.3 eV (Figure 5b). In the visible region, it is seen that Cr provides the highest absorption. All these findings suggest that Cr, Mo, and W doped TiO_2 exhibit better electrical and optical characteristics compared to the undoped case and should also be investigated for other energy applications, beyond photovoltaics and photocatalysis [64].

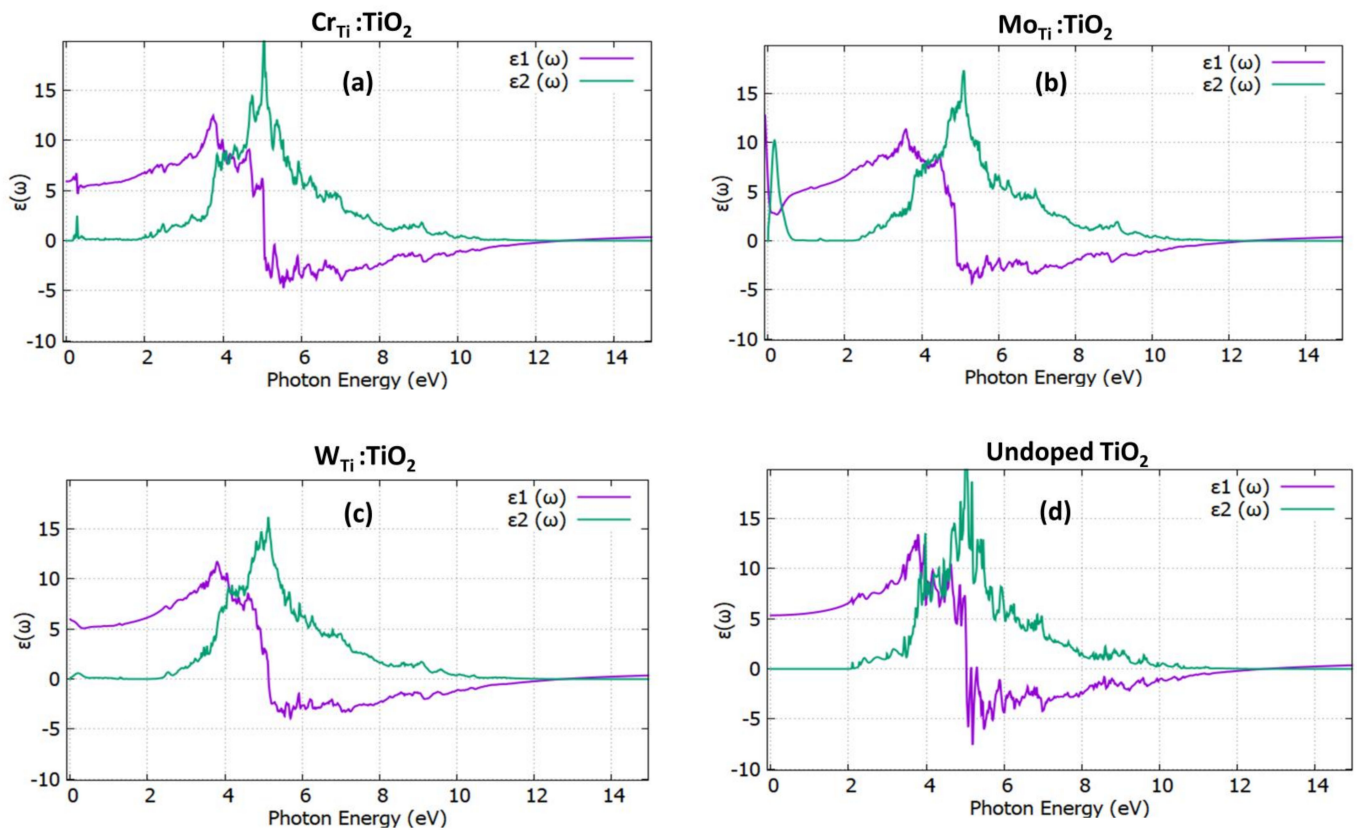


Figure 4. The real $\epsilon_1(\omega)$ and imaginary part $\epsilon_2(\omega)$ of the complex dielectric function for (a) Cr doped TiO_2 , (b) Mo doped TiO_2 , (c) W doped TiO_2 , (d) undoped TiO_2 .

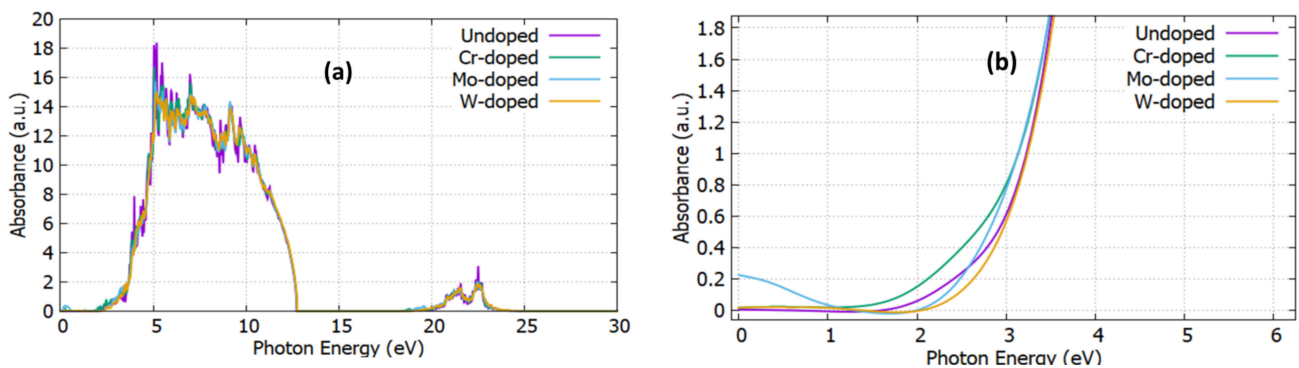


Figure 5. Cont.

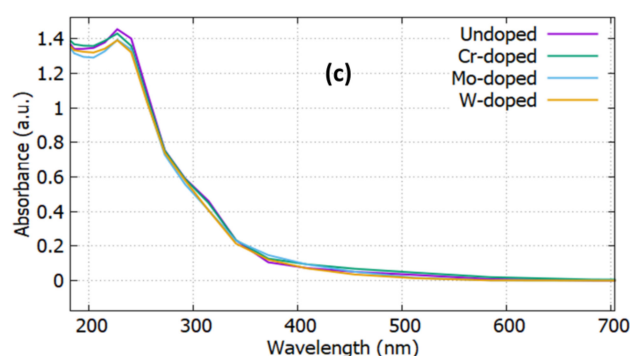


Figure 5. The absorption graph for all the doping cases (a) for all the spectrum (b) for the visible region (1.78–3.1 eV) and (c) as a function of the wavelength.

4. Conclusions

In this work, we used DFT for group 6 (Cr, Mo, W) doped TiO₂ to evaluate the influence of doping on the structural, electronic, and optical properties of TiO₂. In all the cases, it is seen that mid gap states arise, which can be attributed to hybridization of O-p with Ti-d, and a small contribution of Cr-d, Mo-d, and W-d orbitals. These states are beneficial for oxides photocatalytic activities as they reduce the band gap, with the Mo doped TiO₂ achieving the lowest value of 2.77 eV. This value is one of the lowest values achieved for a single doping method. Interestingly, Mo doped TiO₂ is shown to have the highest value of the dielectric constant and refractive index, which makes it the most suitable dopant-candidate for light-harvesting applications.

Author Contributions: P.-P.F. and N.K. performed the DFT calculations; P.-P.F., N.K., M.V., and A.C. wrote the paper; M.V., A.C., and D.D. contributed to the analysis and discussion of the results. All authors have read and agreed to the published version of the manuscript.

Funding: P.-P.F., M.V., D.D., and A.C. are grateful for LRF ICON funding from the Lloyd's Register Foundation charitable foundation for helping to protect life and property by supporting engineering-related education, public engagement, and the application of research. A.C. acknowledges support from the European Union's H2020 Programme under grant agreement No. 824072- HARVESTORE.

Institutional Review Board Statement: Not applicable.

Informed Consent Statement: Not applicable.

Conflicts of Interest: The authors declare no conflict of interest.

References

1. Fujishima, A.; Honda, K. Electrochemical Photolysis of Water at a Semiconductor Electrode. *Nature* **1972**, *238*, 37. [[CrossRef](#)]
2. Gratzel, M. Photoelectrochemical cells. *Nature* **2001**, *414*, 338. [[CrossRef](#)]
3. Asahi, R.; Morikawa, T.; Ohwaki, T.; Aoki, K.; Taga, Y. Visible-light photocatalysis in nitrogen-doped titanium oxides. *Science* **2001**, *293*, 269. [[CrossRef](#)]
4. Khan, S.U.M.; Al-Shahry, M.; Ingler, W.B. Efficient photochemical water splitting by a chemically modified n-TiO₂. *Science* **2002**, *297*, 2243. [[CrossRef](#)] [[PubMed](#)]
5. Russo, S.P.; Grey, I.E.; Wilson, N.C. Nitrogen/hydrogen codoping of anatase: A DFT study. *J. Phys. Chem. C* **2008**, *112*, 7653. [[CrossRef](#)]
6. Yang, H.G.; Sun, C.H.; Qiao, S.Z.; Zou, J.; Liu, G.; Smith, S.C.; Cheng, H.M.; Lu, G.Q. Anatase TiO₂ single crystals with a large percentage of reactive facets. *Nature* **2008**, *453*, 638. [[CrossRef](#)]
7. Gai, Y.; Li, J.; Li, S.-S.; Xia, J.-B.; Wei, S.-H. Design of narrow-gap TiO₂: A passivated codoping approach for enhanced photoelectrochemical activity. *Phys. Rev. Lett.* **2009**, *102*, 036402. [[CrossRef](#)]
8. Vasilopoulou, M.; Georgiadou, D.G.; Soultati, A.; Boukos, N.; Gardelis, S.; Palilis, L.C.; Fakis, M.; Skoulatakis, G.; Kennou, S.; Botzakaki, M.; et al. Atomic-layer-deposited aluminum and zirconium oxides for surface passivation of TiO₂ in high-efficiency organic photovoltaics. *Adv. Energy Mater.* **2014**, *4*, 1400214. [[CrossRef](#)]
9. Sivula, K.; van de Krol, R. Semiconducting materials for photoelectrochemical energy conversion. *Nat. Mater. Rev.* **2016**, *1*, 15010. [[CrossRef](#)]

10. Filippatos, P.P.; Kelaidis, N.; Vasilopoulou, M.; Davazoglou, D.; Chroneos, A. Defect Processes in Halogen Doped SnO₂. *Appl. Sci.* **2021**, *11*, 551. [[CrossRef](#)]
11. Qiu, Y.; Chen, W.; Yang, S. Double-layered photoanodes from variable-size anatase TiO₂ nanospindles: A candidate for high-efficiency dye-sensitized solar cells. *Angew. Chem. Int. Ed.* **2010**, *49*, 3675–3679. [[CrossRef](#)]
12. Ullattil, S.G.; Thelappurath, A.V.; Tadka, S.N.; Kavil, J.; Vijayan, B.K.; Periyat, P. A sol-solvothermal processed 'Black TiO₂' as photoanode material in dye sensitized solar cells. *Sol. Energy* **2017**, *155*, 490–495. [[CrossRef](#)]
13. Govindaraj, R.; Santhosh, N.; Pandian, M.S.; Ramasamy, P.; Sumita, M. Fabrication of stable dye-sensitized solar cell with hydrothermally synthesized titanium dioxide nanorods as a photoanode material. *J. Mater. Sci. Mater. Electron.* **2018**, *29*, 3736–3743. [[CrossRef](#)]
14. Sauvage, F.; Di Fonzo, F.; Li Bassi, A.; Casari, C.S.; Russo, V.; Divitini, G.; Graetzel, M. Hierarchical TiO₂ photoanode for dye-sensitized solar cells. *Nano Lett.* **2010**, *10*, 2562–2567. [[CrossRef](#)] [[PubMed](#)]
15. Zhu, K.; Neale, N.R.; Miedaner, A.; Frank, A.J. Enhanced charge-collection efficiencies and light scattering in dye-sensitized solar cells using oriented TiO₂ nanotubes arrays. *Nano Lett.* **2007**, *7*, 69–74. [[CrossRef](#)]
16. Mor, G.K.; Shankar, K.; Paulose, M.; Varghese, O.K.; Grimes, C.A. Use of highly-ordered TiO₂ nanotube arrays in dye-sensitized solar cells. *Nano Lett.* **2006**, *6*, 215–218. [[CrossRef](#)]
17. Wang, Z.; Fang, J.; Mi, Y.; Zhu, X.; Ren, H.; Liu, X.; Yan, Y. Enhanced performance of perovskite solar cells by ultraviolet-ozone treatment of mesoporous TiO₂. *Appl. Surf. Sci.* **2018**, *436*, 596–602. [[CrossRef](#)]
18. Zhang, D.; Xie, F.; Lin, P.; Choy, W.C. Al-TiO₂ composite-modified single-layer graphene as an efficient transparent cathode for organic solar cells. *ACS Nano* **2013**, *7*, 1740–1747. [[CrossRef](#)]
19. Seo, H.O.; Park, S.Y.; Shim, W.H.; Kim, K.D.; Lee, K.H.; Jo, M.Y.; Kim, J.H.; Lee, E.; Kim, D.W.; Kim, Y.D.; et al. Ultrathin TiO₂ films on ZnO electron-collecting layers of inverted organic solar cell. *J. Phys. Chem. C* **2011**, *115*, 21517–21520. [[CrossRef](#)]
20. Zhang, D.; Choy, W.C.; Xie, F.; Sha, W.E.; Li, X.; Ding, B.; Zhang, K.; Huang, F.; Cao, Y. Plasmonic electrically functionalized TiO₂ for high-performance organic solar cells. *Adv. Funct. Mater.* **2013**, *23*, 4255–4261. [[CrossRef](#)]
21. Lira-Cantu, M.; Chafiq, A.; Faissat, J.; Gonzalez-Valls, I.; Yu, Y. Oxide/polymer interfaces for hybrid and organic solar cells: Anatase vs. Rutile TiO₂. *Sol. Energy Mat. Sol. Cells* **2011**, *95*, 1362–1374. [[CrossRef](#)]
22. Lin, Z.; Jiang, C.; Zhu, C.; Zhang, J. Development of inverted organic solar cells with TiO₂ interface layer by using low-temperature atomic layer deposition. *ACS Appl. Mater. Interfaces* **2013**, *5*, 713–718. [[CrossRef](#)] [[PubMed](#)]
23. Green, M.A.; Ho-Baillie, A.; Snaith, H.J. The emergence of perovskite solar cells. *Nat. Photonics* **2014**, *8*, 506–514. [[CrossRef](#)]
24. Kim, H.S.; Park, N.G. Parameters affecting I–V hysteresis of CH₃NH₃PbI₃ perovskite solar cells: Effects of perovskite crystal size and mesoporous TiO₂ layer. *J. Phys. Chem Lett.* **2014**, *5*, 2927–2934. [[CrossRef](#)]
25. Pathak, S.K.; Abate, A.; Ruckdeschel, P.; Roose, B.; Gödel, K.C.; Vaynzof, Y.; Santhala, A.; Watanabe, S.I.; Hollman, D.J.; Noel, N.; et al. Performance and stability enhancement of dye-sensitized and perovskite solar cells by Al doping of TiO₂. *Adv. Funct. Mater.* **2014**, *24*, 6046–6055. [[CrossRef](#)]
26. Bessekhoad, Y.; Robert, D.; Weber, J.V. Bi₂S₃/TiO₂ and CdS/TiO₂ heterojunctions as an available configuration for photocatalytic degradation of organic pollutant. *J. Photochem. Photobiol. A* **2004**, *163*, 569. [[CrossRef](#)]
27. Vasilopoulou, M.; Kelaidis, N.; Polydorou, E.; Soultati, A.; Davazoglou, D.; Argitis, P.; Papadimitropoulos, G.; Tsikritzis, D.; Kennou, S.; Auras, F.; et al. Hydrogen and nitrogen codoping of anatase TiO₂ for efficiency enhancement in organic solar cells. *Sci. Rep.* **2017**, *7*, 17839. [[CrossRef](#)]
28. Wang, J.; Tafen, D.N.; Lewis, J.P.; Hong, Z.; Manivannan, A.; Zhi, M.; Li, M.; Wu, N. Origin of photocatalytic activity of nitrogen-doped TiO₂ nanobelts. *J. Am. Chem. Soc.* **2009**, *131*, 12290–12297. [[CrossRef](#)]
29. Czoska, A.M.; Livraghi, S.; Chiesa, M.; Giamello, E.; Agnoli, S.; Granozzi, G.; Finazzi, E.; Valentin, C.D.; Pacchioni, G. The nature of defects in fluorine-doped TiO₂. *J. Phys. Chem. C* **2008**, *112*, 8951–8956. [[CrossRef](#)]
30. Zhao, Y.; Li, C.; Liu, X.; Gu, F.; Du, H.L.; Shi, L. Zn-doped TiO₂ nanoparticles with high photocatalytic activity synthesized by hydrogen–oxygen diffusion flame. *Appl. Catal. B Environ.* **2008**, *79*, 208–215. [[CrossRef](#)]
31. Opra, D.P.; Gnedenkov, S.V.; Sokolov, A.A.; Podgorbunsky, A.B.; Ustinov, A.Y.; Mayorov, V.Y.; Kuryavyi, V.G.; Sinebryukhov, S.L. Vanadium-doped TiO₂-B/Anatase Mesoporous Nanotubes with Improved Rate and Cycle Performance for Rechargeable Lithium and Sodium Batteries. *J. Mater. Sci. Technol.* **2020**, *54*, 181–189. [[CrossRef](#)]
32. Sharma, S.D.; Singh, D.; Saini, K.K.; Kant, C.; Sharma, V.; Jain, S.C.; Sharma, C.P. Sol–gel-derived super-hydrophilic nickel doped TiO₂ film as active photo-catalyst. *Appl. Catal. A Gen.* **2006**, *314*, 40–46. [[CrossRef](#)]
33. Kordatos, A.; Kelaidis, N. Chroneos, A. Defect pair formation in fluorine and nitrogen codoped TiO₂. *J. Appl. Phys.* **2018**, *123*, 161510. [[CrossRef](#)]
34. Filippatos, P.P.; Kelaidis, N.; Vasilopoulou, M.; Davazoglou, D.; Lathiotakis, N.N.; Chroneos, A. Defect processes in F and Cl doped anatase TiO₂. *Sci. Rep.* **2019**, *9*, 19970. [[CrossRef](#)]
35. Babu, V.J.; Nair, A.S.; Peining, Z.; Ramakrishna, S. Synthesis and characterization of rice grains like Nitrogen-doped TiO₂ nanostructures by electrospinning–photocatalysis. *Mater. Lett.* **2011**, *65*, 3064–3068. [[CrossRef](#)]
36. Khan, S.; Cho, H.; Kim, D.; Han, S.S.; Lee, K.H.; Cho, S.H.; Song, T.; Choi, H. Defect engineering toward strong photocatalysis of Nb-doped anatase TiO₂: Computational predictions and experimental verifications. *Appl. Catal. B* **2017**, *206*, 520–530. [[CrossRef](#)]
37. Payne, M.C.; Teter, M.P.; Allan, D.C.; Arias, T.A.; Joannopoulos, J.D. Iterative minimization techniques for ab initio total-energy calculations: Molecular dynamics and conjugate gradients. *Rev. Mod. Phys.* **1992**, *64*, 1045. [[CrossRef](#)]

38. Segall, M.D.; Lindan, P.J.D.; Probert, M.J.; Pickard, C.J.; Hasnip, P.J.; Clark, S.J.; Payne, M.C. First-principles simulation: Ideas, illustrations and the CASTEP code. *J. Phys. Condens. Matter* **2002**, *14*, 2717. [[CrossRef](#)]
39. Perdew, J.; Burke, K.; Ernzerhof, M. Generalized gradient approximation made simple. *Phys. Rev. Lett.* **1996**, *77*, 3865. [[CrossRef](#)]
40. Vanderbilt, D. Soft self-consistent pseudopotentials in a generalized eigenvalue formalism. *Phys. Rev. B* **1990**, *41*, 7892. [[CrossRef](#)]
41. Monkhorst, H.J.; Pack, J.D. Special points for Brillouin-zone integrations. *Phys. Rev. B* **1976**, *13*, 5188. [[CrossRef](#)]
42. Kiarri, E.M.; Govender, K.K.; Ndungu, P.G.; Govender, P.P. The generation of charge carriers in semi conductors—A theoretical study. *Chem. Phys. Lett.* **2017**, *678*, 167. [[CrossRef](#)]
43. Liu, C.; Song, Y.; Yu, X.; Liu, J.; Deng, J. Electronic Structure and Optical Absorption Spectra of C–Cr Co-Doped Anatase TiO₂ Based on First Principles. *Phys. Status Solidi B* **2018**, *255*, 1700616. [[CrossRef](#)]
44. Zhang, J.; Deng, M.; Ren, F.; Wu, Y.; Wang, Y. Effects of Mo/W codoping on the visible-light photocatalytic activity of monoclinic BiVO₄ within the GGA+ U framework. *RSC Adv.* **2016**, *6*, 1229. [[CrossRef](#)]
45. Di Valentin, C.; Pacchioni, G. Trends in non-metal doping of anatase TiO₂: B, C, N and F. *Catal. Today* **2013**, *206*, 12–18. [[CrossRef](#)]
46. Samsudin, E.M.; Hamid, S.B.A. Effect of band gap engineering in anionic-doped TiO₂ photocatalyst. *Appl. Surf. Sci.* **2017**, *391*, 326–336. [[CrossRef](#)]
47. Nagpal, P.; Klimov, V.I. Role of mid-gap states in charge transport and photoconductivity in semiconductor nanocrystal films. *Nat. Commun.* **2011**, *2*, 486. [[CrossRef](#)] [[PubMed](#)]
48. Yang, K.; Dai, Y.; Huang, B. Density Functional Characterization of the Electronic Structure and Visible-Light Absorption of Cr-Doped Anatase TiO₂. *ChemPhysChem* **2009**, *10*, 2327. [[CrossRef](#)] [[PubMed](#)]
49. Gönüllü, Y.; Haidry, A.A.; Saruhan, B. Nanotubular Cr-doped TiO₂ for use as high-temperature NO₂ gas sensor. *Sens. Actuators B Chem.* **2015**, *217*, 78. [[CrossRef](#)]
50. Luttrell, T.; Halpegamage, S.; Tao, J.; Kramer, A.; Sutter, E.; Batzill, M. Why is anatase a better photocatalyst than rutile?—Model studies on epitaxial TiO₂ films. *Sci. Rep.* **2014**, *4*, 4043. [[CrossRef](#)] [[PubMed](#)]
51. Kelaidis, N.; Kordatos, A.; Christopoulos, S.-R.G.; Chroneos, A. A roadmap of strain in doped anatase TiO₂. *Sci. Rep.* **2018**, *8*, 12790. [[CrossRef](#)]
52. Takaoka, G.H.; Nose, T.; Kawashita, M. Photocatalytic properties of Cr-doped TiO₂ films prepared by oxygen cluster ion beam assisted deposition. *Vacuum* **2008**, *83*, 679. [[CrossRef](#)]
53. Yu, X.; Hou, T.; Sun, X.; Li, Y. The influence of defects on Mo-doped TiO₂ by first-principles studies. *ChemPhysChem* **2012**, *13*, 1514. [[CrossRef](#)]
54. Yu, C.J.; Yu, J.; Ho, W.; Jiang, Z.; Zhang, L. Effects of F-doping on the photocatalytic activity and microstructures of nanocrystalline TiO₂ powders. *Chem. Mater.* **2002**, *14*, 3808. [[CrossRef](#)]
55. Kubacka, A.; Colón, G.; Fernández-García, M. Cationic (V, Mo, Nb, W) doping of TiO₂–anatase: A real alternative for visible light-driven photocatalysts. *Catal. Today* **2009**, *143*, 286. [[CrossRef](#)]
56. Kubacka, A.; Colon, G.; Garcia, M. N-and/or W-(co) doped TiO₂-anatase catalysts: Effect of the calcination treatment on photoactivity. *Appl. Catal. B Environ.* **2010**, *9*, 238. [[CrossRef](#)]
57. Samat, M.H.; Ali, A.M.M.; Taib, M.F.M.; Hassan, O.H.; Yahya, M.Z.A. Hubbard U calculations on optical properties of 3d transition metal oxide TiO₂. *Res. Phys.* **2016**, *6*, 891.
58. Abdel-Aziz, M.M.; Yahia, I.S.; Wahab, L.A.; Fadel, M.; Afifi, M.A. Determination and analysis of dispersive optical constant of TiO₂ and Ti₂O₃ thin films. *Appl. Surf. Sci.* **2006**, *252*, 8163. [[CrossRef](#)]
59. Yu, X.; Li, C.; Ling, Y.; Tang, T.A.; Wu, Q.; Kong, J. First principles calculations of electronic and optical properties of Mo-doped rutile TiO₂. *J. Alloys Compd.* **2010**, *507*, 33. [[CrossRef](#)]
60. Khan, M.; Xu, J.; Chen, N.; Cao, W. Electronic and optical properties of pure and Mo doped anatase TiO₂ using GGA and GGA+ U calculations. *Phys. B* **2012**, *407*, 3610. [[CrossRef](#)]
61. Mergel, D. Modeling thin TiO₂ films of various densities as an effective optical medium. *Thin Solid Films* **2001**, *397*, 216. [[CrossRef](#)]
62. Hajjaji, A.; Labidi, A.; Gaidi, M.; Ben Rabha, M.; Smirani, R.; Bejaoui, A.; Bessais, B.; El Khakani, M.A. Structural, optical and sensing properties of Cr-doped TiO₂ thin films. *J. Sens. Lett.* **2011**, *9*, 1697. [[CrossRef](#)]
63. Lin, S.S. Properties of heavily W-doped TiO₂ films deposited on Al₂O₃-deposited glass by simultaneous rf and dc magnetron sputtering. *Ceram. Int.* **2014**, *40*, 217. [[CrossRef](#)]
64. Opra, D.P.; Gnedenkov, S.V.; Sinebryukhov, S.L. Recent efforts in design of TiO₂(B) anodes for high-rate lithium-ion batteries: A review. *J. Power Sources* **2019**, *442*, 227225. [[CrossRef](#)]